Long wavelength astrophysics

by

Liam Dean Connor

A thesis submitted in conformity with the requirements
for the degree of Doctor of Philosophy
Graduate Department of Astronomy and Astrophysics
University of Toronto

Abstract

Long wavelength astrophysics

Liam Dean Connor
Doctor of Philosophy
Graduate Department of Astronomy and Astrophysics
University of Toronto
2016

Acknowledgements

Contents

List of Tables

Chapter 1

Beamforming

1.1 Chapter Overview

In an era when electric fields can be sampled billions of times per second, radio telescopes are becoming more and more digital. While the cost of constructing large single-dish telescopes is not expected to decrease substantially, the cost of building large computing clusters is, which makes it economically and strategically sensible to point one's telescope in software, as with digital beamforming. Beamforming is particularly essential to CHIME. The pulsar back-end will rely on brute-force beamforming in order to track ten sources at a time, 24-7. The FRB experiment will FFT-beamform to generate 1024 fan-beams, in order to search them in real time for radio transients. And the cosmology experiment has always left itself the option of beamforming, whose computing cost scales as $N \log N$, as an alternative to the full N^2 correlation. This chapter outlines the basic theory behind digital beamforming, and describes the commissioning of the first beamformer on CHIME Pathfinder. This includes the synthesis of several different software packages, the implementation of an early scheduler, and an automated point-source calibration daemon that removes drifting instrumental gains in real-time. We will also detail early pulsar work and the creation of an ongoing VLBI FRB search between the DRAO and ARO. The latter will include constraints on α.

1.2 Introduction

Beamforming is a signal processing technique that allows for spatial filtering, and has greatly benefited a diverse set of fields from radar and wireless communications to radio astronomy.

1.3 Theory and Implementation

By coherently combining the voltages of a multi-element array, sensitivity can be allocated to small regions of the sky and the array's effective forward gain can be increased. The signal from each antenna, x_n, is multiplied by a complex weight whose phases, ϕ_n, are chosen to maximally destructively interfere radio waves in all directions but the desired pointing. The signals from all antennas are then combined to give the formed-beam voltage stream, X_{BF}.

$$X_{\mathrm{BF}} = \sum_{n=1}^{N} a_n e^{i\phi_n} x_n \tag{1.1}$$

Here a_n are real numbers that can be used as amplitude weightings for the antennas. If we define a more general complex weighting, $w_n \equiv a_n e^{i\phi_n}$, and switch to vector notation, Eq. 1.1 becomes,

$$X_{\mathrm{BF}} = \mathbf{w}\,\mathbf{x}^{\mathrm{T}}. \tag{1.2}$$

In general, X_{BF} and $\mathbf{x}^{\mathrm{T}}$ will be functions of time and frequency. This is also true for $\mathbf{w}$, unless one needs a static, non-tracking beam – which is the case for the CHIME Pathfinder's transient search, described in Sect. 1.5. We can write this explicitly as follows.

$$\mathbf{w}_{\mathrm{t}\nu} = \left(a_1(\nu)e^{i\phi_1(\nu)},\, a_2(\nu)e^{i\phi_2(\nu)}, \dots,\, a_N(\nu)e^{i\phi_N(\nu)}\right) \tag{1.3}$$

$$\mathbf{x}_{\mathrm{t}\nu} = (x_1(\mathrm{t},\nu),\, \mathrm{x}_2(\mathrm{t},\nu), ...,\, \mathrm{x_N}(\mathrm{t},\nu)) \tag{1.4}$$

The voltage stream is then effectively squared and integrated to give a visibility stream. In the case of CHIME, X_{BF} corresponds to a single polarization so to get the full Stokes information one must compute the north-south polarization's autocorrelation, the east-west autocorrelation, and their cross-correlation. The Stokes vector can be written as,

$$\begin{pmatrix} I \\ Q \\ U \\ V \end{pmatrix} = \begin{pmatrix} X_{\mathrm{ew}}X_{\mathrm{ew}}^* + X_{\mathrm{ns}}X_{\mathrm{ns}}^* \\ X_{\mathrm{ew}}X_{\mathrm{ew}}^* - X_{\mathrm{ns}}X_{\mathrm{ns}}^* \\ \Re e(X_{\mathrm{ew}}X_{\mathrm{ns}}^*) \\ \Im m(X_{\mathrm{ew}}X_{\mathrm{ns}}^*) \end{pmatrix}. \tag{1.5}$$

1.3.1 Geometric phase

We now need to calculate ϕ_n across the array. Ignoring instrumental phases for now, one can compute the geometric phases for an antenna by projecting its position vector, $\mathbf{d}_n$, onto the pointing vector, $\hat{\mathbf{k}}$. This gives,

$$\phi_n = \frac{2\pi}{\lambda}\,\mathbf{d}_n \cdot \hat{\mathbf{k}}, \tag{1.6}$$

where we have taken $\mathbf{d}_n$ to be the baseline vector between feed n and an arbitrary reference point, and ϕ_n is the corresponding phase difference. A sketch for this is shown in Fig. 1.5.2 on page 14.

To calculate the projection $\mathbf{d}_n \cdot \hat{\mathbf{k}}$, we need to go from celestial coordinates, in this case equatorial, to geographic coordinates. This requires only a source location, an observer location, and an observing time. For the latter we use local sidereal time (LST), which is the RA of the local meridian. This can be determined by an observer's longitude and a time, e.g. a Coordinated Universal Time (UTC). A source's hour angle is simply the difference between LST and its RA,

$$HA = LST - RA. \tag{1.7}$$

We use the standard interferometric (u, v, w) coordinate system to describe our baseline vector, $\mathbf{d}_n$. This is a right-handed coordinate system where u (east-west) and v (north-south) are in the plane whose normal is the zenith, and w measures the vertical direction (Thompson et al., 1986). They are defined in numbers of wavelengths, with $u = d_{\mathrm{ew}}/\lambda$, $v = d_{\mathrm{ns}}/\lambda$, and $w = d_{\mathrm{vert}}/\lambda$. Eq. 1.6 can be expanded as,

$$\begin{aligned}
\phi_n &= 2\pi\,(u, v, w) \cdot \hat{\mathbf{k}} && (1.8)\\
&= 2\pi\left(u\,\hat{\mathbf{u}} \cdot \hat{\mathbf{k}} + v\,\hat{\mathbf{v}} \cdot \hat{\mathbf{k}} + w\,\hat{\mathbf{w}} \cdot \hat{\mathbf{k}}\right), && (1.9)
\end{aligned}$$

where each projection component can be obtained using spherical trigonometry. Though we do not go through the derivation here, it is given by the following product,

$$\mathbf{d}_n \cdot \hat{\mathbf{k}} = \lambda \begin{pmatrix} u, & v, & w \end{pmatrix} \cdot \begin{pmatrix} -\cos\delta \sin HA \\ \cos(lat)\sin\delta - \sin(lat)\cos\delta\cos HA \\ \sin(lat)\sin\delta + \cos(lat)\cos\delta\cos HA \end{pmatrix}. \tag{1.10}$$

These phases are not only essential to beamforming but also for the fringestopping process, which is ubiquitous in interferometric analysis and is descibed in Sect. 1.4.1.

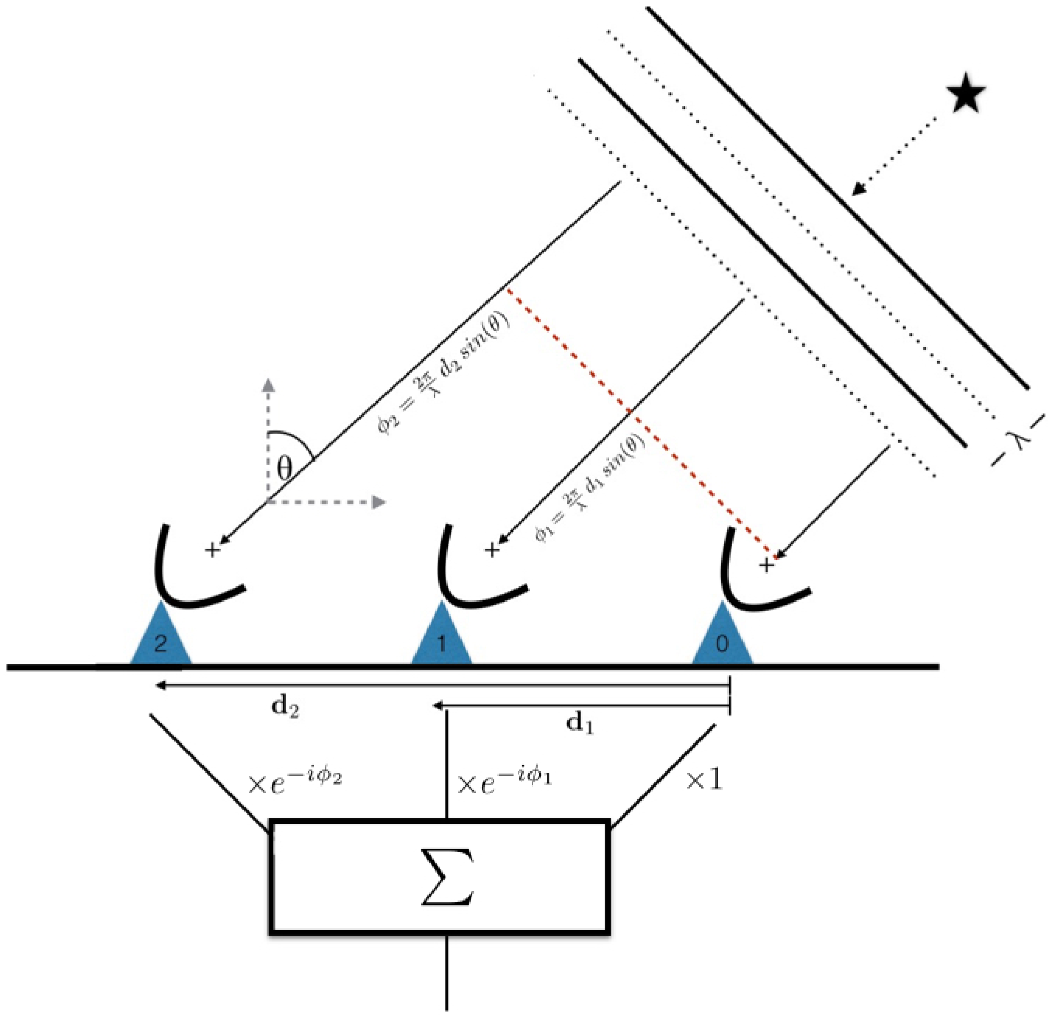

Figure 1.1: Diagrammatic example of a three-element beamformer. The wavefront from a far-field point-source arrives at each antenna at different times, but the delay is calculable given an array configuration and a direction to the object. Complex weights can be applied to each antenna's voltage time-stream to account for the geometric delay, allowing for the signals to be summed coherently.

1.4 Pathfinder beamformer

1.4.1 Instrumental phases

In a real experiment, if the voltages from each antenna, x_n, are summed without any adjustment from those written in Eq 1.1, one should only expect noise and not a coherent beam. This is because we have assumed the wavefront's differential time-of-arrival across at array is the same time delay seen by the correlator. In fact each signal is further delayed by multiple steps in the signal chain, often randomly. Digital phases in the electronics can be added by the LNAs and FLAs; coaxial cables, whose lengths vary by

Variable	**Coordinate**
δ	Source declination
RA	Source right ascention
LST	Local sidereal time
HA	Source hour angle
alt	Source altitude
az	Source azimuth
lat	Telescope latitude
lon	Telescope longitude

up to a meter, can rotate the signal by multiple radians. Therefore in order to coherently sum across the array and beamform, the instrumental phases must be removed. If e_n is the true electric field on the sky as seen by each feed, then the thing we measure is the on-sky signal altered by an effective gain, g_n, and a noise term, n_n.

$$x_n = g_n e_n + n_n \tag{1.11}$$

We have lumped several terms into $g_n = |g_n|e^{i\phi_{g_n}}$, which is composed of a pointing-dependent beam term and any complex gain introduced once light hits the cylinder. Since we care primarily about the phase, we can decompose $\arg(g_n)$ as,

$$\phi_{g_n} = \phi_{\text{beam}} + \phi_{\text{an}} + \phi_{\text{e}} + \phi_{\text{fpga}} \tag{1.12}$$

where ϕ_{beam} is the beam's phase for a given pointing, ϕ_{an} comes from the analogue chain (dual-pol feed, coax, etc.), ϕ_{e} is any phase introduced in the electronics, and ϕ_{fpga} are phases applied in the F-engine.

Since the instrumental phases are effectively random, the simplest way to remove them is to solve for them empirically, usually from a point-source on the sky. Using the visibility definition in Eq 1.16, one can evaluate that all-sky integral assuming the sky's electric field is produced by a single point-source. This is tantamount to a delta function at a single direction on the sky.

$$V^{\text{ps}}_{m,n} = \int d^2\hat{\mathbf{k}}\, g_m(\hat{\mathbf{k}})\, g^*_n(\hat{\mathbf{k}})\, e_m(\hat{\mathbf{k}})e^*_n(\hat{\mathbf{k}})\, \delta(\hat{\mathbf{k}} - \hat{\mathbf{k}}_{\text{ps}}) \tag{1.13}$$

$$= g_m(\hat{\mathbf{k}}_{\text{ps}})\, g^*_n(\hat{\mathbf{k}}_{\text{ps}})\, e_m(\hat{\mathbf{k}}_{\text{ps}})e^*_n(\hat{\mathbf{k}}_{\text{ps}}) \tag{1.14}$$

In these equations $\hat{\mathbf{k}}_{\text{ps}}$ is the only direction on the sky with a source in it — an approximation whose validity we will discuss below — and δ is a Kronecker delta function.

$$V^{\text{ps}}_{m,n} = \tag{1.15}$$

$$V_{m,n} = \int d^2\hat{\mathbf{k}}\, g_m(\hat{\mathbf{k}})\, g^*_n(\hat{\mathbf{k}})\, e_m(\hat{\mathbf{k}}) e^*_n(\hat{\mathbf{k}}) \tag{1.16}$$

If we explicitly write the phase information of the sky's electric field, we can use

$$e_m(\hat{\mathbf{k}}) e^*_n(\hat{\mathbf{k}}) = T(\hat{\mathbf{k}}) e^{2\pi\, i\, \hat{\mathbf{k}}\cdot\mathbf{d}_{mn}}, \tag{1.17}$$

subbing into Eq. 1.13

$$V_{m,n} = \int d^2\hat{\mathbf{k}}\, g_m(\hat{\mathbf{k}})\, g^*_n(\hat{\mathbf{k}})\, T(\hat{\mathbf{k}}) e^{2\pi\, i\, \hat{\mathbf{k}}\cdot\mathbf{d}_{mn}} \tag{1.18}$$

Therefore a single correlation can be written as an intensity multiplied by a phase factor that is determined by the source direction's projection onto that correlation's baseline. Since that phase factor is calculable via Eq. 1.10, it can be removed in a process called "fringestopping". The data can be inspected visually quite easily, since a transiting point-source will fringe as a function of time at a rate corresponding to the projected baseline length, but should not after fringestopping is applied. This is demonstrated with an inter-cylinder Cygnus A transit in Fig. 1.4.1.

The visibilities we measure can be thought of as the upper triangle of an $N \times N$ complex Hermitian matrix, $\mathbf{V}$. This is simply the outer product of the signal vector, $\mathbf{x}$, with its Hermitian conjugate.

$$\mathbf{V} = \mathbf{x}\mathbf{x}^\dagger \approx \begin{pmatrix} |g_0|^2\, e_0^2 & \cdots & & \\ & & g_n g_m^* e_n e_m^* & \\ & \ddots & & \\ & & & \\ & & & |g_N|^2\, e_N^2 \end{pmatrix} \tag{1.19}$$

If the sky is composed of a single point-source then this matrix will be rank one, i.e. there is only one non-zero eigenvalue. One can see this by referring to Eq. 1.17 and noting that if the data has been fringestopped, then the phase component (which is different for each correlation) goes away and the sky temperature (which is the same) can be factored

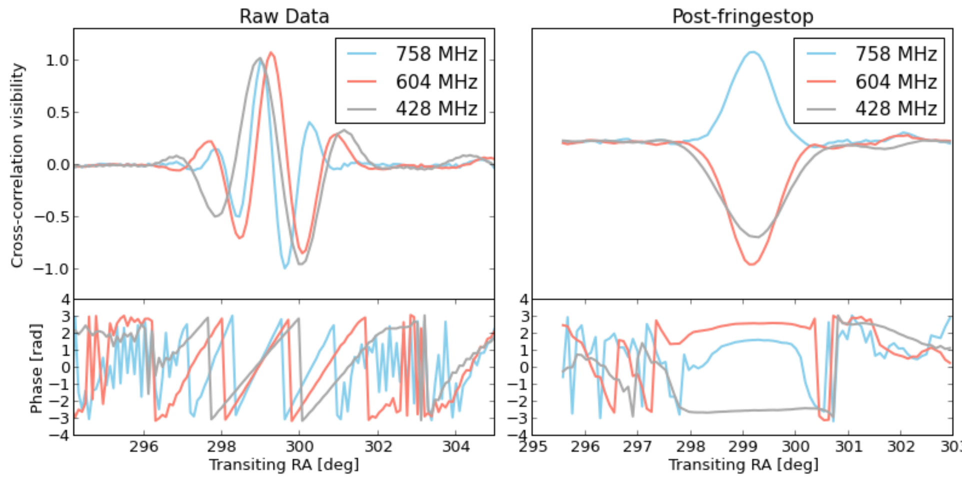

Figure 1.2: An example of the fringestopping process that is necessary for gain calibration off of a transiting point-source. Since the phase of a visibility will have a time- and frequency-dependent component, the measured correlation will fringe as the earth rotates in a chromatic way. This effect can be removed by multiplying each visibility by $e^{-i\phi_{m,n}(\mathrm{t},\nu)}$, as determined by Eq. 1.10. The top left panel shows the raw correlation between feeds 1 and 129 as a function of transiting RA, which are of the same polarization but on opposite cylinders, separated by 21 m. We plot three different frequencies. The panel below the top left shows the same complex visibility's phase. The slope, or fringe-rate, decreases at lower frequencies, as expected. The right panel show the same data after running it through the fringestopping pipeline. Though the resulting phases are near flat, implying that the baseline is no long fringeing, the visibilities are not purely real; this is because there are residual instrumental phases. These phases can be solved for using an eigendecomposition now that the array is phased up to a single point-source.

out of Eq. 1.19, which becomes

$$\mathbf{V} = T(\hat{\mathbf{k}})\,\mathbf{g}\mathbf{g}^{\dagger}. \tag{1.20}$$

Therefore by diagonalizing the correlation matrix $\mathbf{V}$ we get a complex eigenvector corresponding to the largest eigenvalue, and that eigenvector is proportional to the gain vector $\mathbf{g}$. The phase of this eigenvector will be an estimate for the instrumental phases, ϕ_{g_n}, up to some unknown global offset. The goodness of this calibration depends on the validity of our assumption that the correlation matrix is rank one. We can estimate the error on the calibration solution as the ratio of the second largest eigenvalue, λ_2, to the largest, λ_1. For typical frequencies we get values of $\frac{\lambda_2}{\lambda_1} \sim 3\%$.

These algorithms have been implemented in a pre-beamforming pipeline written in `Python`. Each day a point-source transit is fringestopped and a calibration solution is solved for at each frequency. The source chosen depends on the solar time of its transit: Since the sun is extraordinarily bright in our band it will be in our side-lobes as long as it is above the horizon, so the transit has to be at night for good calibration solutions. Historically, we have used Cygnus A in the spring and summer, Cassiopeia A in the summer and fall, and Tau A in the winter. Whatever we calibrate off of, the phases of that solution are written to pickle files that are readable by the Pathfinder's FPGAs. The FPGA then applies complex gains after channelization, which in theory should provide the beamforming kernel with voltages whose phases are purely geometric.

1.4.2 First coherent light

Although the majority of the back-end was written within a couple of months, the beamformer required substantial on-sky testing and subsequent debugging. One important debugging tool came from utilizing the equivalence of the summed-and-squared high-cadence data that was produced by the beamformer with the full N^2 integrated data. This is true because the correlation step does not erase any fundamental information about the electric field. The latter is nominally taken with ~ 21 second time samples for 32,896 correlation products coming from 256 feeds. The former is a sum over the feeds which can be integrated in time arbitrarily after squaring. Ignoring the time rebinning for a moment, we can write the squared formed beam as,

$$
\begin{aligned}
X_{\mathrm{BF}}X_{\mathrm{BF}}^* &= (w_1x_1 + w_2x_2 + ... + w_Nx_N)(w_1x_1 + w_2x_2 + ... + w_Nx_N)^* && (1.21)\\
&= |w_1|^2|x_1|^2 + ... + |w_N|^2|x_N|^2 + ... + w_1w_2^*x_1x_2^* + w_2w_1^*x_2x_1^* + ..., && (1.22)
\end{aligned}
$$

where, as before, w_n are the complex weights applied in the beamformer and x_n is a voltage stream from antenna n. This can be rewritten as the sum of the auto correlations and twice the real part of the recorded cross-correlations.

$$
X_{\mathrm{BF}}X_{\mathrm{BF}}^* = \sum_{n\leq N} |w_n|^2 V_{n,n} + 2 \sum_{\substack{n,m\leq N\\ n<m}} \Re e\{W_{n,m}V_{n,m}\} \tag{1.23}
$$

In this equation we have let $W_{n,m} \equiv w_n w_m^*$. Since the correlation matrix is Hermitian, its top and bottom triangles are redundant and one needs only to record $\frac{1}{2}N(N+1)$ of the N^2 pairwise products. If we wrote all pairwise correlations, we would simply need to sum the correlation matrix after applying the relevant weights, i.e. summing after the Hadamard product, $\mathbf{W} \circ \mathbf{V}$. This is identical to Eq. 1.23 if both matrices are Hermitian.

Using the equivalence we have just described, one can compare the output of the beamformer to the N^2 visibilities after applying complex weights and summing the correlations. This is effectively off-line beamforming, though the cadence is too slow for the science goals of the real back-end, namely studying the time-variable sky. As a first test, we would form a stationary beam with only two feeds and let a bright point-source like Cas A drift through, producing a fringe pattern. We would then take the corresponding Cas A transit from the correlated "cosmology" acquisition, using Eq. 1.23 and giving only non-zero weights to the two relevant feeds, and check if the two fringe patterns were identical. We carried out a series of tests of escalating complexity, for example including more feeds in the sum, updating phases in real-time in order to track sources, and deliberately switching the weights with their conjugate to see if the fringe direction changed. Through these tests several bugs were discovered, including spherical trigonometry errors in the phase calculations and a disagreement between one piece of code's definition of LST.

The final hurdle was more fundamental to CHIME's architecture, though in principle it should not affect the cosmology experiment. It was found through early pulsar observations that the beamformer was only summing coherently when the instrumental phases that are removed in the FPGAs are solved for with the lower-triangle of the correlation matrix. In other words, instrumental phases were not properly removed in the correlator unless they were applied as $e^{+i\phi_{gn}}$ instead of $e^{-i\phi_{gn}}$, as one would expect. The perplexing thing was that in two years of analyzing

the visibilities output by the correlator, nobody noticed a error in the sign-convention. And indeed, when we started to look at the phase of the raw visibilities, we found the argument of an east-west baseline increases with time, which is what one expects from an upper-triangle correlator. This apparent paradox was solved by discovering *two* sign errors, on in the F-engine and one in the X-engine, that effectively cancel each other out, but only if both are applied.

Our digitizers sample at 800 MHz, taking advantage of the observing band between 400-800 MHz being in the second Nyquist zone . However, when we channelize the incoming time-stream data in the FPGAs, the complex conjugation associated with the aliased second Nyquist zone was not considered during the Fourier transform. Therefore the channelized voltages leave the F-engine with an opposite sign in the exponential.

When they are correlated in the X-engine it is also done in reverse order as,

$$V_{n,m} = x_n^* x_m, \tag{1.24}$$

as opposed to the upper-triangle correlation described by **?**,

$$V_{n,m} = x_n x_m^*. \tag{1.25}$$

The second sign convention error does not affect the beamformed output, since that data stream is never correlated. We therefore needed to account for this for the back-end to work. An example of an early verification of the beamformer's sign convention and the first successful tracking observation is shown in Fig. 1.4.2. The collaboration has decided to keep these sign conventions as is and make note of it going forward, rather than re-write any low-level software.

1.5 FRB VLBI search

In 1967 Canada achieved an historic feat by doing the first ever successful VLBI observation. The fringes were obtained between DRAO and ARO, with a baseline of 3,074 km (Broten et al., 1967). This result was given a "Milestone" award from The Institute of Electrical and Electronics Engineers (IEEE), which was also awarded for the inception of the Internet, transmission of transatlantic radio signals, and the discovery of Maxwell's equations (IEE, ????). We have attempted to recreate the same VLBI baseline, but instead of using the considerable spatial resolution on quasars as in 1967, we are attempting to localize FRBs.

1.5.1 Motivation

The CHIME Pathfinder is meant to have only one synthetic beam. Its purpose is primarily to act as a test-bed for the more powerful pulsar and FRB back-ends that will be attached to the full four-cylinder CHIME. However since the Pathfinder is on sky at all times and the beamformer we have built does not interrupt the ongoing cosmology acquisition, we decided to build a preliminary FRB search. We also have as many as three other telescopes onto which we can mount CHIME feeds and observe in our band: the Algonquin Radio Observatory (ARO), the John A. Galt 26m, and the Green Bank 140ft telescope. This would allow for the first ever VLBI detection of an FRB.

This is interesting for a few reasons. From a development standpoint it allows us to

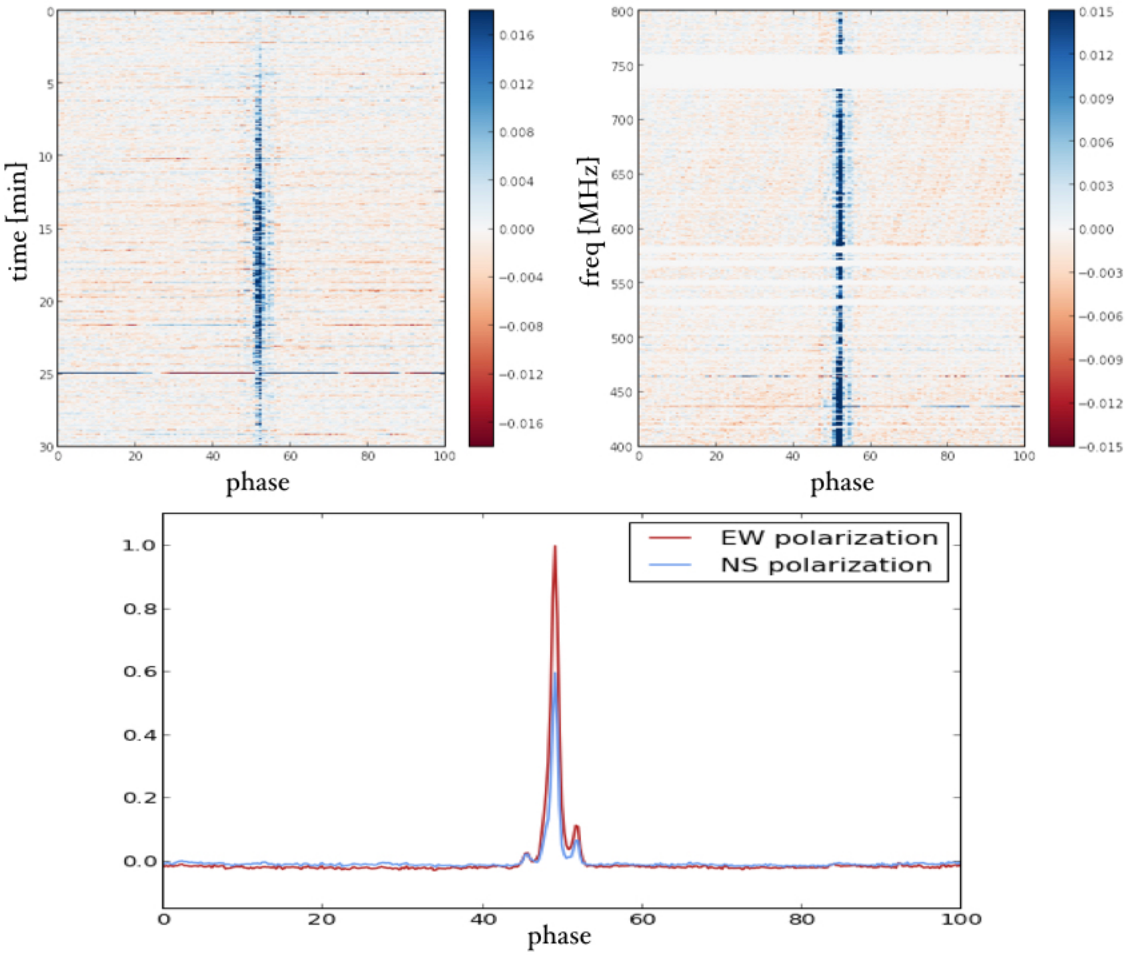

Figure 1.3: First coherent pulsar observations with CHIME. This brief observation of B0329+54 provided us with an idea of the instrument's sensitivity and polarization response. Perhaps more significantly, it taught us that that our X-engine is a lower-triangle correlator, rather than upper-triangle like we thought, and that our F-engine *also* conjugates with the opposite sign. *top left:* waterfall plot of the pulsar's Stokes I profile over the ∼30 minutes when the source enters then exits our beam. *top right:* frequency vs. phase Stokes I, integrated over roughly 15 minutes. *bottom:* time- and frequency-averaged pulse profile for the two polarizations autocorrelations. The difference between the east-west and north-south beams give an estimate for Stokes Q, which includes both intrinsic polarization (∼ 10% for this source) and instrumental leakage.

understand better various stages of the CHIME-FRB pipeline, including the rate of RFI false-positives, our algorithm's search efficiency, and specs on the regularity and precision of instrumental gain removal. It will also give us a good sense of how the real CHIME beams behave on the sky. Perhaps most interestingly, we could reasonably expect to see a burst after several months of observing, hopefully in coincidence with the telescopes previously mentioned. We could therefore not only detect an FRB with sub-arcsecond resolution, but also would the first source in our band, at 400-800 MHz, including full polarization information. While searching for fast radio bursts, we could also find RRATs and new slow pulsars, since a significant fraction of the Galaxy transits each day.

1.5.2 Implementation

We have had a working beamforming back-end on the CHIME Pathfinder since October 2015. It has been used primarily for short tracking pulsar observations, but had stability issues on timescales of ∼days, meaning we could not run it for long periods without interfering with the regular cosmology acquisition. However in the past several months a number of new features were added that allow not only long-term beamforming captures, but also transient searching.

A real-time, multithreaded acquisition code that takes in the VDIF packets coming out of the X-engine, and rearranges them to either be written to disk or search for FRBs[1]. Attached to this packet reader was a tree-dedispersion search code, some of which had been used before on Green Bank 100m data and a real-time ARO search[2]. The CHIME acquisition software `kotekan` was altered in a number of ways, fixing the long-term stability issues in the beamforming kernel. These systems were synthesized into a real-time transient search back-end that has been on sky since May 2016. It is outlined in Fig. 1.5.2 on page 14.

Since CHIME is a transit telescope with a long north-south beam, our formed beam is effectively confined to the meridian. This means we must choose an optimal declination on which to park the beam. As a sanity check, we spent $\sim$ 10 days pointed at the declination of pulsar B0329+54, which is the brightest switching source in the northern sky in our band. It is dispersed with 26.833 pc cm^{-3} and its individual pulses are bright enough to detect, meaning our tree-dedispersion algorithm ought to find its individual pulses. During the ten or so minutes that the source is in our beam each day, the algorithm looks at time blocks of 100 seconds, searches for DMs between 10-2000 pc cm^{-3} with widths between 1-100 ms, and looks for peaks above 8σ. If it finds something it "triggers" and writes out an image file containing the peak in DM / arrival time space, a dedispersed waterfall plot, a dedispersed pulse profile, and a fluence frequency spectrum. An example of the B0329+54 is shown in Fig.??. It also writes `numpy` arrays

[1]https://github.com/kmsmith137/ch_vdif_assembler
[2]https://github.com/kiyo-masui/burst_search

containing the squared and summed intensity data. It then moves on to the next block of 100 seconds, overlapping with the previous one by 18 seconds.

1.5.3 Results

As we discuss in chapter **??**, there is a large uncertainty in the FRB rate between 400-800 MHz. There is even greater uncertainty in the expected rate for a telescope like the CHIME Pathfinder. This is because at this time all FRBs have been detected with large-collecting area, highly sensitive single-dish telescopes (GBT, Parkes, and Arecibo). Therefore in order to extrapolate the rate estimates on to the Pathfinder, which does not have much collecting area and whose beam is quite large, one needs to know the underlying flux distribution. As we will show in Eq. **??**, the rate depends on the product of the telescope's field-of-view (FoV) and a thermal sensitivity term. This scales $\propto A^{-1}A^{\gamma}$, where A is collecting area and γ is the FRB flux distribution's power-law index, which is 3/2 if FRBs are non-cosmological and Euclidean. If $\gamma < 1$, as is expected in the cosmological FRB scenario, then small telescopes are actually advantageous over large single-pixel telescopes since the beamsize becomes more important.

With a dish like the Pathfinder the rate is roughly 10 times higher if $\gamma \approx 0.8$ (cosmological scenario) compared to the Euclidean scenario. This is because its relatively low sensitivity per steradian requires there be large numbers of very bright bursts, which one gets from a flat distribution.

1.6 Conclusion

Acknowledgements

We thank Andre Recnik

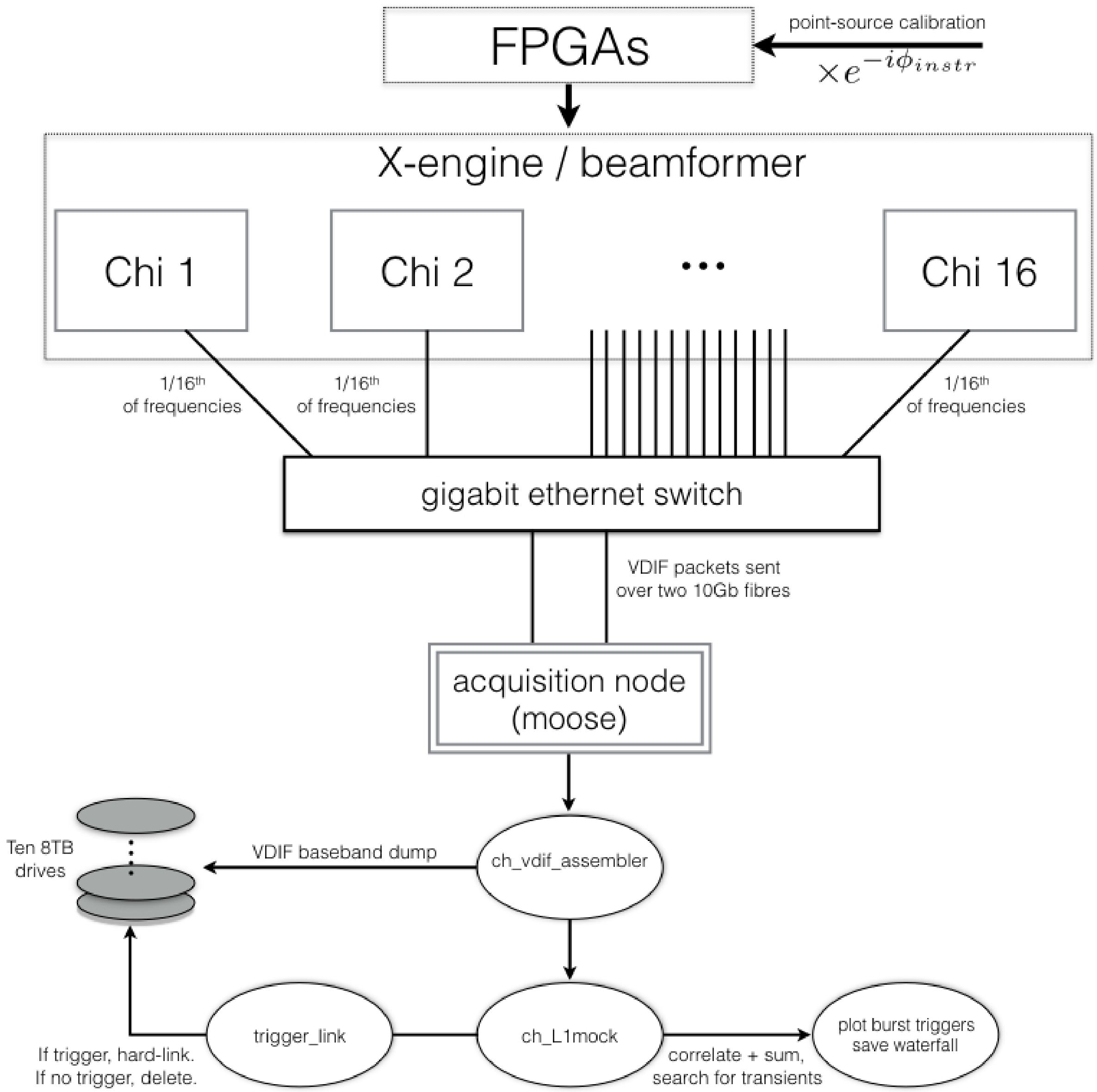

Figure 1.4: Block diagram of the beamforming back-end on CHIME Pathfinder. A calibration solution is obtained from a bright point-source transit, the phases of which are fed into the FPGAs where they are applied as a digital gain. All antenna signals are then sent the X-engine, comprised of 16 GPU nodes. Each node applies geometric phases then sums the voltage stream across all antennas with the same polarization. The two resultant beams are then sent to our acquisition machine `moose` as `VDIF` packets, where a multi-threaded capture code, `ch_vdif_assembler`. At this point the baseband data are either written to disk as scrambled baseband `VDIF`, or they are reorganized in time and frequency. The ordered data are searched for FRBs after squaring and integrating to ∼millisecond cadence using a tree-dedispersion algorithm. If there is a trigger, then the corresponding baseband data is hard-linked. Old files that haven't been hard-linked are deleted periodically.

Bibliography

????, IEEE Milestone award, http://ethw.org/Milestones:List_of_IEEE_Milestones, accessed: 2016-06-13

Broten, N. W., Locke, J. L., Legg, T. H., McLeish, C. W., & Richards, R. S. 1967, Nature, 215, 38

Thompson, A. R., Moran, J. M., & Swenson, G. W. 1986, Interferometry and synthesis in radio astronomy